RESEARCH ARTICLE

ADVANCED
INTELLIGENT
SYSTEMS
Open Access

www.advintellsyst.com

# 2D Shape Estimation of a Pneumatic-Driven Soft Finger with a Large Bending Angle Based on Learning from Two Sensing Modalities

*Jianxiong Hao, Zhiqiang Zhang, Shuxin Wang, and Chaoyang Shi**

A shape estimation method that utilizes two sensing modalities of a customized fiber Bragg grating (FBG) sensor and a commercial air pressure sensor for a pneumatically driven soft finger with an extensive bending angle range based on an artificial neural network model is proposed. The proposed FBG sensor utilizes two tiny nitinol rods as a backbone to attach the long-grating FBG element fiber, enabling high strain transfer, shape sensing for large bending deformation, and preventing chirping failure and fiber sliding when bending. Its distal end is set free to slide and synchronizes with the extended length and reflects shapes for large bending deformation (up to 320° with a linearity of 99.96%), while its proximal end is fixed. The small packaged sensor unit enables modular design, easy assembly, and high repeatability with negligible effects on the soft finger's bending performances. The artificial neural network model is utilized to process the input of two sensing modalities, reducing errors from material nonlinearity, fabrication, and assembly of soft fingers while improving shape estimation's accuracy and transferability with average errors of 0.90 mm (0.69%) and 1.55 mm (1.19%) for whole shape and distal end position, respectively. Preliminary experiments also verify the potential for pressing force prediction and hardness recognition.

## 1. Introduction

In recent years, soft robots have been thriving and introduced in wearable and implantable medical devices, rehabilitation robots,[1–3] minimally invasive surgery,[4–6] and multifunctional graspers to operate complex and fragile objects,[7–10] due to the merits of excellent compliance, flexibility, and environmental adaptability.[2,11] However, these merits also bring considerable challenges to the precise control of soft robots.[12] To achieve accurate closed-loop motion control and safe interaction with the environment, it is essential to implement real-time shape estimation.[13] However, the shape of soft robots is heavily influenced by both internal drives and external loadings. Coupled with their complicated intrinsic deformation, nonlinear behaviors of the fabrication materials and apparent motion hysteresis result in significant complexity in accuracy shape estimation.[12,14,15] Meanwhile, the direct attachment of traditional commercial sensors will affect the motion of the soft robots due to either high stiffness or large volume, or poor stretchability, making it difficult for them to be integrated into soft robots.[12] Several approaches have been implemented to estimate the shape of soft robots to address these challenges. They can be primarily classified into the direct measurement method and indirect measurement method.

The direct measurement methods typically collect the curvature data of soft robots in the configuration space through customized sensors and then directly obtain the shape information in the task space. These methods usually involve applying a series of flexible sensors along the body of a soft robot to provide discrete shape information.[16] According to the sensing mechanism, the common flexible and stretchable sensors mainly consist of capacitive sensors,[17–19] resistive sensors,[10,20–23] optical sensors,[24–28] magnetic sensors,[29–31] and so on. However, the stretchable sensors typically suffer from nonlinearity, hysteresis, and nonuniform fabrication quality, resulting in limited accuracy and measurement frequency, a tedious calibration process, and a lack of transferability.[20,32–35] When measuring the large bending deformation, these sensors are prone to be highly nonlinear due to the significant and coupling stress distribution characteristics, resulting in inaccurate and even failed measurement results. The inextensible sheets of rigid and discretized elements (such as printed circuit boards, IMU) joined by known axes of rotation have been also applied to realize shape sensing.[36,37] However, they are typically utilized for large deformable objects (such as basketballs, large-sized robotic arms)

J. Hao, S. Wang, C. Shi
Key Laboratory of Mechanism Theory and Equipment Design of Ministry of Education
School of Mechanical Engineering
Tianjin University
Tianjin 300072, China
E-mail: chaoyang.shi@tju.edu.cn

Z. Zhang
School of Electronic and Electrical Engineering
University of Leeds
Leeds LS2 9JT, UK

The ORCID identification number(s) for the author(s) of this article can be found under https://doi.org/10.1002/aisy.202200324.

**ADVANCED
SCIENCE NEWS**

www.advancedsciencenews.com

**ADVANCED
INTELLIGENT
SYSTEMS**
Open Access

www.advintellsyst.com

due to the rigid and large sensing elements. These disadvantages make it difficult for this method to be applied to small-sized soft manipulators. The multicore optical fibers have been arranged along the neutral axis of the flexible endoscopes to realize 3D shape sensing.[38,39] Such a sensor arrangement can avoid the position and length change issue of the neutral axis for continuum manipulators. However, it is difficult to obtain the exact neutral axis/plane position of the pneu-net soft finger because of its asymmetric and complex design and the unavoidable errors in the process of manual fabrication and assembly. Moreover, the neutral axis/plane can be changed during the large nonlinear deformation. Therefore, this method that places the fiber along the neutral axis for the continuum robot[38,39] involves more complex problems in estimating the change in length and cannot be directly for soft fingers. It is notable that the direct application of fiber Bragg grating (FBG)-based optical shape sensing in pneumatic-driven soft robots remains challenging due to the large fiber slippage after assembly and the limited stretchable property of the optical fiber.[40] The large bending angles and significant deformation of the pneumatic-driven soft actuators are typically much larger than that of other types of soft robots and continuum robots.[12,41] These drawbacks make shape estimation challenging, especially for soft robots with large deformation.

Without utilizing customized sensors, the indirect measurement methods typically collect the driving data from the actuator space, such as air pressure values through commercial sensors, and then generate the shape information indirectly based on the mapping relationship between the actuator and task space. This mapping relationship can be obtained by the model-based method or learning-based method. For the model-based method, the kinetostatic model[42–45] (e.g., based on Cosserat rod theory or Euler–Bernoulli principle) and finite-element analysis (FEA) method[46] are popularly performed. However, these model parameters are typically time varying and difficult to identify accurately due to the inherent nonlinearity of material constitutive relation and the geometric deformation nonlinearity influenced by the complicated and unpredictable internal drives and external loadings. These drawbacks typically result in inaccurate and time-consuming solutions or unstable controllers, making it difficult to be utilized for the shape estimation of soft robots. In comparison, the learning-based algorithms are independent of the physical model and the configuration of soft robots[47,48] and have become an emerging and potential approach for shape estimation. However, the current implementations mainly utilize the existing commercial sensors (e.g., tension/force sensors) that are difficult to be integrated with soft robots or the limited sensory sources for data collection.[12] Multiple sensing modalities are demanding for these learning-based methods to obtain sufficient input data to further improve the shape estimation accuracy and enhance the robustness in the presence of errors caused by manufacturing, movements of the soft robots, and robot integration.[49] The optical fiber-based sensing modalities have been increasingly introduced and combined with the learning-based methods to derive a continuous shape estimation.[50,51] However, the embedded optical fiber-based shape sensing in soft robots remains challenging due to the considerable fiber slippage after assembly and the limited stretchable property of the optical fiber and suffers from a limited bending/motion range and low transferability.

To address these difficulties, this work proposes a shape estimation method that utilizes two sensing modalities for a pneumatically driven soft finger with a large bending angle range based on an artificial neural network (ANN) model. These two kinds of sensor units include a customized FBG sensor from the configuration space and a commercial air pressure sensor input from the actuator space. The proposed FBG sensor unit design empowers large bending curvature information detection with high repeatability of the sensory data and avoids the typical FBG chirping failure and fiber sliding when bending. It supports easy assembly on soft manipulators with negligible effects on their bending performances. The distal end is freely set to slide inside the channel and synchronize with the extended length to depress the coupling of bending and elongation and reflect the actual shape. The ANN model has been utilized to process the input data from two types of sensors to improve the accuracy and robustness of the proposed approach. Experiments have been performed to investigate the shape estimation capacity and preliminary force perception on the designed soft manipulator. The transferability of the proposed method has also been investigated without requiring a model training process using either a newly built soft manipulator or a newly assembled FBG unit.

## 2. Experimental Section

### 2.1. Hardware Configuration of the Proposed System

The experimental framework was designed to achieve accurate control and real-time feedback of the soft finger based on learning from multi-input sensing modalities, as illustrated in **Figure 1**. The hardware configuration consisted of a microcontroller, a stepping motor, an air cylinder driven by a linear stage, a customized soft finger, and two sensors for shape estimation. The microcontroller (Arduino Mega 2560, Arduino LLC, Brescia, Italy) read control signals from the host PC and controlled the stepping motor. The stepper motor ran at 20 Hz to actuate the air cylinder (inner diameter = 25 mm, length = 150 mm) via the linear stage to drive the soft finger to bend. An air pressure sensor (PCM380, Suzhou Xuansheng Instrument Technology Ltd., Suzhou, CN) with a sensing accuracy of 10 Pa was applied to provide the pressure data with an update rate of 20 Hz. A customized FBG sensing unit was proposed and integrated along the sidewall of the soft finger to reflect the deformation strain. An FBG interrogator (MOI-SI155, Micron Optics Inc., Georgia, USA) operated at 1000 Hz with a wavelength resolution of 1 pm to collect the corresponding reflective FBG central wavelength shift values. These two kinds of sensing sources for both internal and external sensing in the actuator and configuration spaces were applied for shape reconstruction and preliminary contact prediction. A camera (resolution = 1920 × 1080) was employed for ground truth collection with the red marker line attached along with the soft finger.

### 2.2. Structural Design and Optimization of the Soft Finger

The pneu-net configuration with a series of chambers connected by channels was adopted to design the soft finger[52] (**Figure 2**a). The pneu-net allowed the soft finger to deform into an
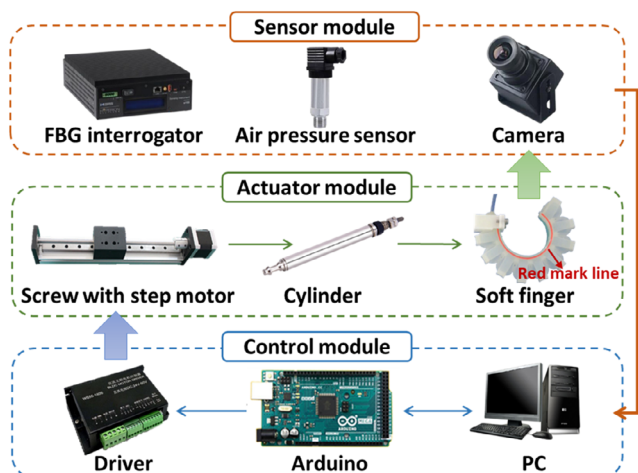
ADVANCED
SCIENCE NEWS
www.advancedsciencenews.com

ADVANCED
INTELLIGENT
SYSTEMS
Open Access
www.advintellsyst.com

**Figure 1.** The hardware configuration of the proposed platform.

approximate circle with uniform inflation of nearly all chambers, thus benefiting uniform pressure distribution and a closely constant curvature deformation. However, due to the super-elastic property of the silicone material, the internal pressure of the soft finger had a nonmonotonic relationship with deformation,[53] and an excessive radial deformation was also generate under high internal pressure. These disadvantages obviously affect the constant curvature performance of soft fingers and reduce the modelling accuracy based on the constant curvature assumption, which is widely used in different shape estimation methods, and increase the complexity of bending deformation control. Thus, the design parameters of the pneu-net configuration had to be further optimized to form a monotonic pressure–deformation relationship and limit the radial deformation.

This measure aimed to achieve better constant curvature performance with lower pressure and less material deformation for shape estimation. Two important parameters which are the chamber width and top thickness heavily affect the bending performance and radial deformation, so they were selected for optimization.[46,54] The FEA method was utilized to determine the optimal solutions for design optimization (Figure 2b,c), and the result and the detailed parameters are illustrated in Figure 2a. (The process of soft finger parameter optimization is detailed in Section S1, Supporting Information).

### 2.3. Design and Assembly of the Proposed FBG Sensor Unit

The proposed FBG sensor unit consisted of two nitinol rods (Jiangyin Haolu Ni–Ti New Materials Ltd., Wuxi, CN) with the same diameter of 0.5 mm and a length of 140 mm, and one optical fiber inscribed with a 15 mm long-grating FBG element (Beijing Tongwei Technology Ltd., Beijing, CN) (**Figure 3**a). The two nitinol rods served as the backbone to carry the FBG fiber with a diameter of around 0.2 mm, and they were bonded together by 401 quick-drying glue (Shenzhen Tegu New Materials Ltd., Shenzhen, CN) to form a sensor unit. The utilized long-grating FBG fabrication method involved exposing a photosensitive fiber to an interference fringe pattern in UV light through a phase mask.[55,56] The grating spacing of this FBG element was about 1 μm. A flexible tube with a diameter of 1.4 mm was employed as a sensor channel to carry the FBG sensor unit for easy assembly with the soft finger. The proximal end of this FBG sensor unit was fixed onto the sensor channel, and the distal end was set free and could slide inside the channel. Thus, when the soft finger experienced a relatively large deformation, this design supported the FBG sensor unit to slip and synchronize with the extended length and reflected its elongated shape.
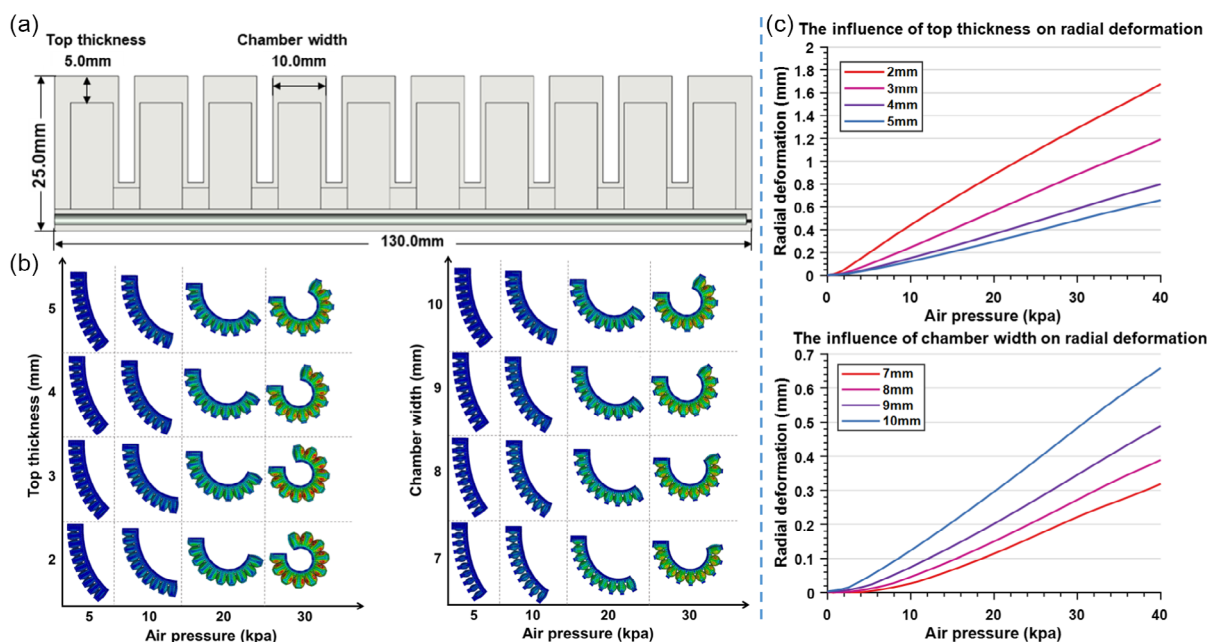


**Figure 2.** a) The construction and parameters of the pneu-net soft finger. b) The influence of top thickness and chamber width on bending performance. c) The influence of top thickness and chamber width on radial deformation.

The proposed configuration with two nitinol rods supported improved strain transfer efficiency from the soft finger to the embedded FBG element and enhanced fiber antitwisting capacity and further addressed the following common difficulties associated with FBG casting inside the soft robots. First, when the soft finger experienced a relatively large bending angle or deformation, the direct casting fiber inside the soft finger could be slippery and torsional, due to the limited adhesive force. Second, the large bending deformation commonly induced the FBG sensor to cross the soft finger's neutral surface. This resulted in the stress change from the stretching state to the compression state and introduced an unpredictable wavelength shift, which cannot reflect the actual shape.

Meanwhile, to realize the large bending deformation estimation and avoid the FBG chirping failure,[57] a long-grating FBG element with a length of 15 mm was adopted for strain collection instead of the commonly utilized short FBG element. The same soft finger was integrated with these two sensor units to validate their performances (Figure 3). Compared with the short-grating FBG element (Figure 3b), the bending angle for the long-grating FBG was obviously larger (Figure 3c) when the chirping occurred. This usage was of great help for effective data collection, especially for the soft robots that required a large curvature deformation and induced the slippery and chirping failure for the short-grating FBG element.

## 2.4. Preliminary Performance Tests of the Soft Finger Integrated with the FBG Sensor Unit

In order to verify the linearity of the proposed FBG sensor unit, a preliminary calibration experiment was carried out based on a multichannel calibration board (**Figure 4**a). The wavelength of the FBG sensor unit under bending with a curvature radius of 40–200 mm (interval = 20 mm) was collected. As shown in Figure 4b, the linearity error was 0.69%, indicating an excellent linearity of the proposed FBG sensor unit (Figure 4b). The theoretical calculation was performed to show that the bending stiffness of the proposed sensor unit was much smaller than that of the pneu-net soft finger. The bending stiffness of the proposed FBG sensor unit can be calculated as $5.09\,\text{N}\,\text{cm}^2$ based on the theory of mechanics of materials. The bending stiffness of the pneu-net soft fingers typically ranged within $79.42–96.5\,\text{N}\,\text{cm}^2$.[44] (The detailed derivation process is added in Section S2, Supporting Information). The large difference between them indicated that the FBG sensor unit can generate a neglectable effect on the bending deformation of the soft finger. The bending performances for the soft finger with and without the proposed FBG unit were experimentally compared for validation (Figure 4c). These results showed a small relative error of 1.69% on the tip position for these two cases, validating the minimum effects induced by the assembly of the FBG sensor unit on the soft finger. The results showed that the proposed assembly method with a flexible tube can make the FBG sensor unit fit the shape of the soft finger without affecting its bending deformation. Meanwhile, the employed nitinol rod was thin and possessed hyperelastic properties, and the FBG fiber was small and flexible. They generated relatively small rebound forces compared with the large internal driving forces inside the soft finger. Furthermore, the repeatability of the soft finger assembled with the integrated FBG sensor was conducted. The bending experiments were repeated for five cycles, and the FBG wavelength and
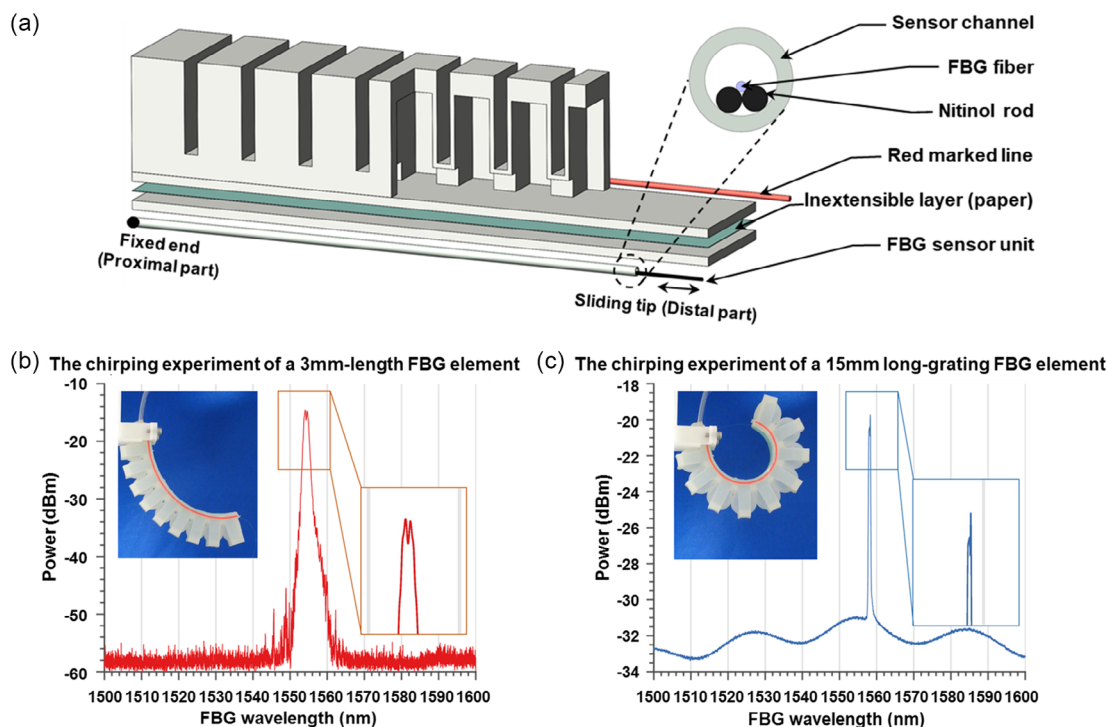


**Figure 3.** a) Detailed structure of the designed soft finger and FBG sensor unit. b) The chirping experiment of a 3 mm-long FBG element. c) The chirping experiment of a long-grating FBG element with a length of 15 mm.
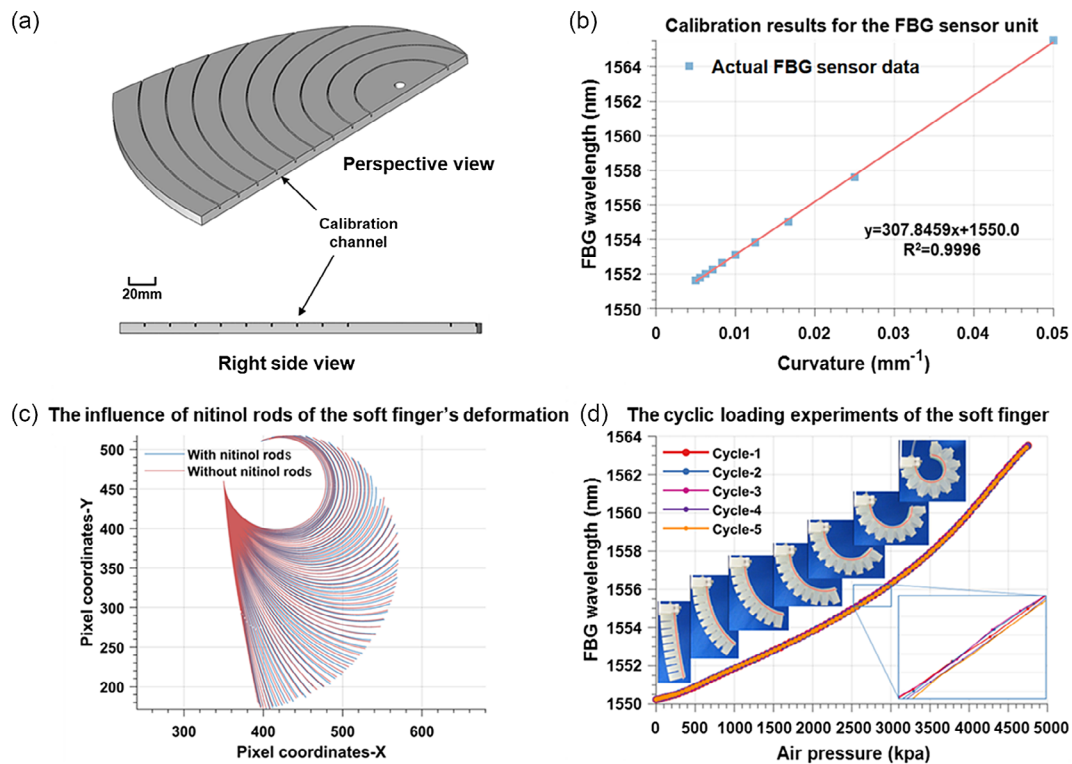
**Figure 4.** a) The multichannel calibration board. b) Calibration results for the FBG sensor unit. c) The influence of nitinol rods of the soft finger's deformation. d) The cyclic loading experiments of the soft finger.

the air pressure were recorded (Figure 4d). The measured pressure–wavelength curves demonstrated a repeatable precision error of less than 80 pm on FBG wavelength (0.6% of the total workspace) in the same air pressure and a small hysteresis for the integrated FBG sensor unit. These curves demonstrated a strictly monotonic mapping relationship, making it an excellent candidate for the following shape estimation.

## 2.5. Multi-Input ANN Model for Shape Estimation

The air pressure parameter in the actuator space and the FBG wavelength parameter in the configuration space were utilized to provide dual-modality inputs for a multilayer perceptron-based (MLP) model ANN1, aiming at comprehensively approaching the complex nonlinear mapping relationship with the whole shape of the soft finger in the task space, as illustrated in **Figure 5** and **6**. The ANN1 model was established with TensorFlow 2.0 (Google LLC, California, USA), and the details of the ANN1 model are shown in **Table 1**. The air pressure and FBG data can be directly obtained from the corresponding sensor units during the training data collection. The ground truth data of the finger shape can be collected by imaging processing on the attached red maker line and then sampling the feature points. Bezier curve was utilized to acquire the actual bending shape of the soft finger from a large number of discrete feature points obtained from images. Meanwhile, the two arcs of constant curvature curves can simplify the curve parameters into four feature point coordinates along the Bezier curve, balancing the accuracy and calculation
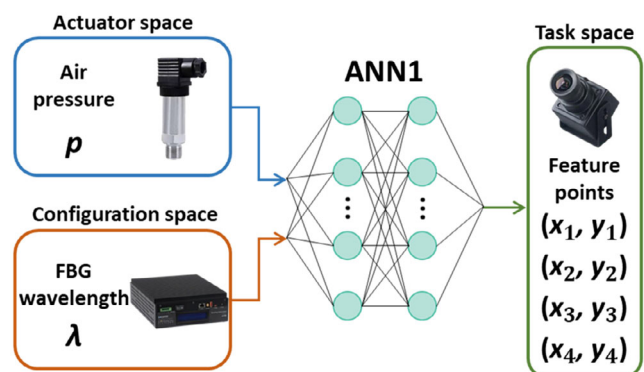


**Figure 5.** The presented multi-input ANN1 model for shape reconstruction.

complexity. Five points (one fixed point and four feature points) were collected and then further fit by two-segment circular arcs to form the whole shape of the soft finger (Figure 6). (The workflow of feature point extraction and curve reconstruction is presented in Section S3, Supporting Information).

The curvature data measured by the FBG sensor unit in configuration space can directly deduce the shape of the task space through geometric relations and will not be affected by the material nonlinearity, manufacturing, and assembly errors. The air pressure data obtained by the commercial air pressure of the actuator space was stable and not easily disturbed by the external
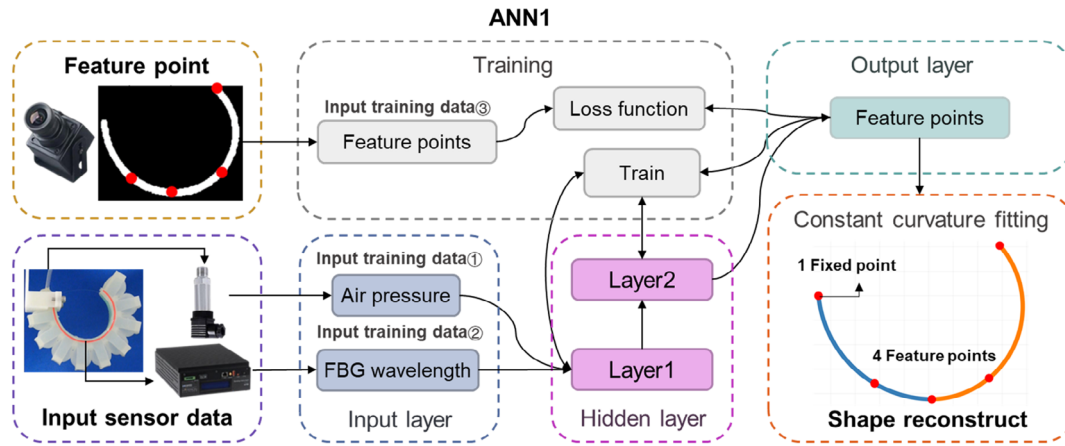
**Figure 6.** The presented shape reconstruction method based on the ANN1 model.

**Table 1.** Detailed parameters of the ANN1 model.

| Neural network model | Hidden layer number | Input nodes | Layer1 nodes | Layer2 nodes | Output nodes | Activation function | Learning rate | Training epochs |
|---|---|---|---|---|---|---|---|---|
| ANN1 | 2 | 2 | 64 | 64 | 8 | Relu | 0.2 | 4352 |

environment. Thus, the usage of the multi-input model can improve the accuracy and robustness of shape estimation. Meanwhile, it can also compensate for model uncertainties caused by sensing noises, manufacturing and assembly errors, and further effectively improve the model's transferability.

## 3. Results

### 3.1. Data Collection and Offline Training for the Multi-Input ANN Model

The soft finger was driven by the stepping motor to deform and bend from 0° to a maximum angle of 320°, due to its mechanical design limitation. The corresponding air pressure data, the central wavelength shift values from the FBG sensor, and the shape of the red mark line were recorded for data training. The training data set of 500 groups has been collected from an inflation and deflation cycle and grouped into a training set (80%) and a test set (20%) for training and testing the proposed ANN1 model. The loss function is defined as the sum of distances between the four predicted feature points and the actual values.

$$\mathrm{Loss}_1 = \sum_{i=1}^{4} \sqrt{(x_i - \overline{x}_i)^2 + (y_i - \overline{y}_i)^2} \tag{1}$$

where $x_i$ and $y_i$ denote the predicted coordinate of the feature point; $\overline{x}_i$ and $\overline{y}_i$ imply the actual coordinate of the feature point. The average error values for the whole shape and the distal tip position of offline training are 0.86 and 1.51 mm, respectively. They account for 0.66% and 1.16% of the total length of the soft finger, validating the effectiveness of the proposed ANN1 model.

### 3.2. Real-Time Shape Estimation of the Soft Finger in Free Space

The air pressure and the wavelength shift value from the FBG sensor were recorded in real time with a frame rate of 20 Hz. The trained ANN1 model was applied online with the same frame rate to reconstruct the whole shape and estimate the distal tip position when the soft finger was controlled to bend from 0° to 320° in the free space with a constant inflation speed (**Figure 7**). The shape estimation of six typical bending cases is illustrated in Figure 7. The average error values for the distal tip position and the whole shape estimation during the whole process are 1.55 and 0.90 mm (Figure 7). They account for 1.19% and 0.69% of the total length of the soft finger, demonstrating the high accuracy and effectiveness of the proposed shape estimation method.

### 3.3. Transferability of the Proposed Shape Estimation Method

To verify the transferability of the proposed shape estimation method, two experiments were carried out with a newly fabricated soft finger and a newly assembled FBG sensor unit respectively. The previously obtained ANN1 model was directly utilized to predict the tip position and whole shape of the soft finger without data training, and the error results are quantified, as shown in **Figure 8**a,b. The average error values for the distal tip position and the whole shape estimation of the newly fabricated soft finger embedded with the previously FBG sensor unit are 2.35 mm (1.81% of its length) and 1.46 mm (1.12% of its length) respectively (Figure 8a). Meanwhile, the corresponding average error values for the soft finger embedded with the newly made FBG sensor unit are 1.78 mm (1.27% of its length) and 1.09 mm (0.78% of its length) respectively (Figure 8b). The estimation error values for the new soft finger and FBG sensor unit are slightly higher than the previous configuration results of 1.55 mm and 0.90 mm in Figure 7, but still with high accuracy and stability. Therefore, the proposed method with multiple inputs can significantly reduce manual fabrication and assembly errors, and model uncertainties, demonstrating excellent transferability for shape estimation.
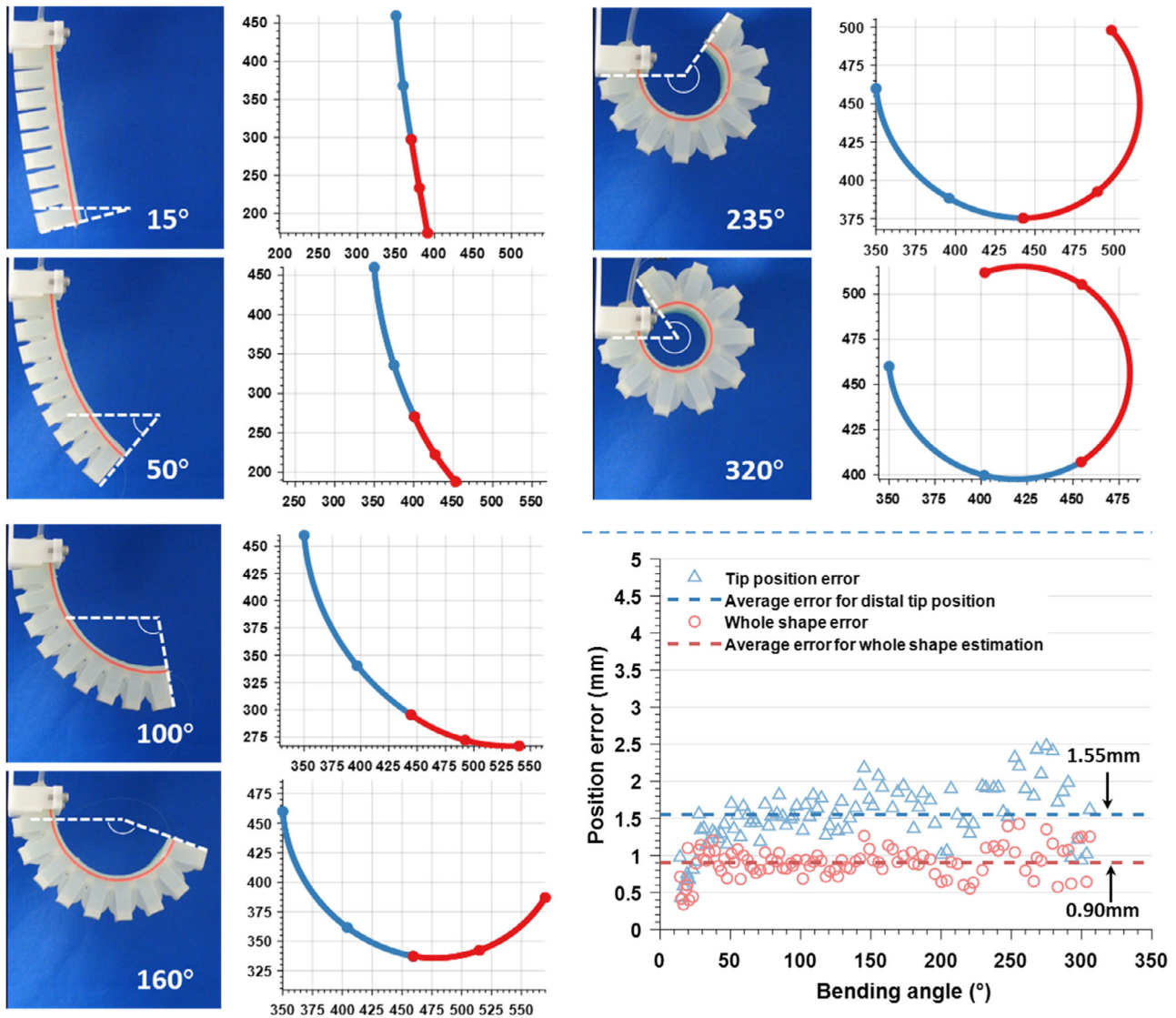
**ADVANCED
SCIENCE NEWS**

www.advancedsciencenews.com

**ADVANCED
INTELLIGENT
SYSTEMS**

www.advintellsyst.com

**Figure 7.** Shape estimation results and errors at different bending angles.

The shape estimation performance comparisons between the proposed ANN model (ANN1) with dual-sensing modalities inputs and the models with only single-sensing modality input (air pressure or FBG wavelength) were quantified by experiments (Figure 8c,d). The experimental results show that the average error values for the whole shape estimation on two soft fingers of the ANNp (6.87 and 9.99 mm respectively) and ANNw (3.03 and 4.58 mm respectively) are much lower than that of the ANN1 model (0.90 and 1.46 mm, respectively). Meanwhile, the average error values for the whole shape estimation of the ANNp and ANNw are increased by 3.12 and 1.55 mm, respectively, when they are applied to the newly fabricated soft finger. These values are much larger than the error increase of the ANN1 model (0.56 mm). Therefore, the ANN model (ANN1) with dual-sensing modalities inputs can effectively produce higher shape estimation accuracy and robustness and stronger transferability than the method with single-sensing modality input.

### 3.4. Preliminary Detection of Interferences Caused by the Contact Forces

The proposed shape estimation method with dual-sensing modalities can also be extended to achieve preliminary contact force perception with the MLP-based model ANN2 (**Figure 9**a). The loss function of the ANN2 is defined as the squared error between the predicted FBG wavelength and the actual values

$$Loss_2 = |(w - \overline{w})| \tag{2}$$

where $w$ and $\overline{w}$ denote the predicted and actual FBG wavelength respectively, and the details of the ANN2 model are shown in **Table 2**. The current algorithm utilizes the difference between the predicted FBG wavelength $\lambda_p$ and the actual FBG wavelength $\lambda_a$ to preliminary detect the contact forces, as shown in Equation (3).
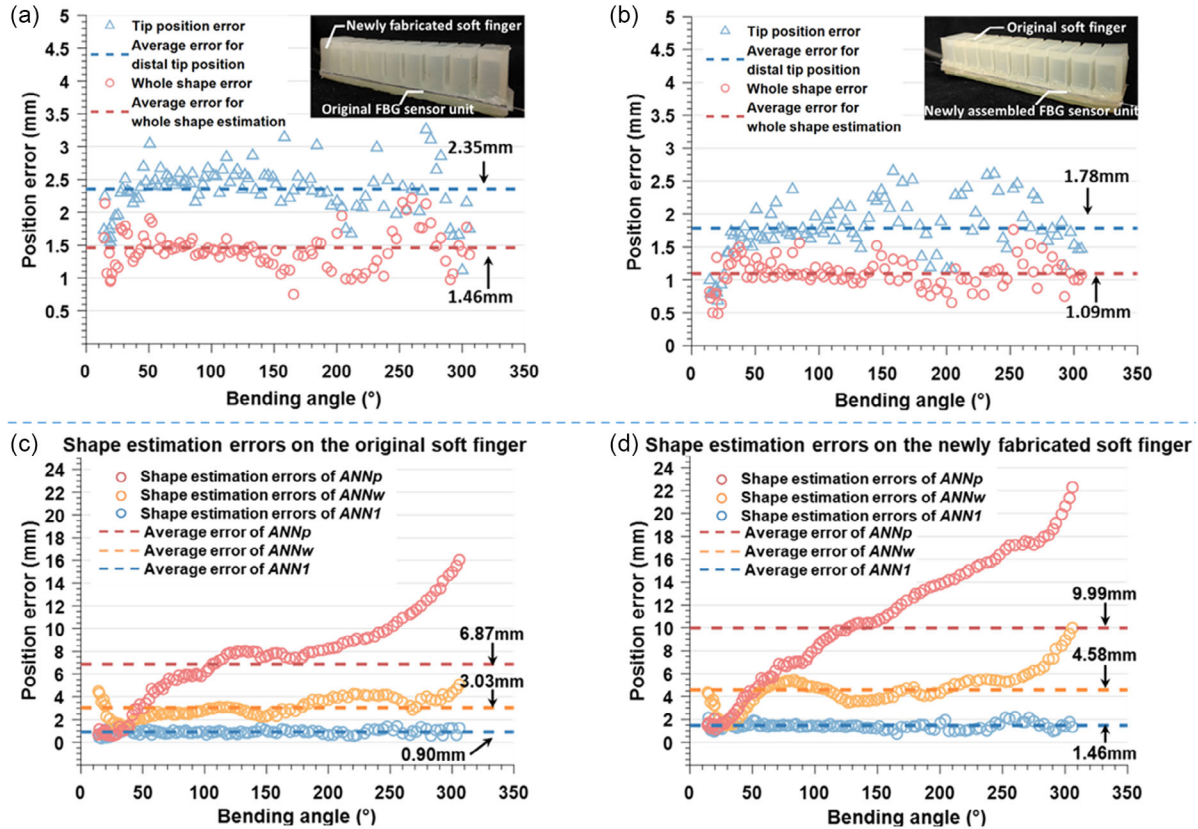
**Figure 8.** a) Real-time error values of the shape estimation for the newly fabricated soft finger at different bending angles. b) Real-time error values of the shape estimation for the newly assembled FBG sensor unit at different bending angles. c) Shape estimation errors of three different ANN models on the original soft finger. d) Shape estimation errors of three different ANN models on the newly fabricated soft finger.

$$\Delta\lambda = \lambda_p - \lambda_a \tag{3}$$

where $\lambda_p$ is predicted by the ANN2 model using the air pressure data in a free state and $\lambda_a$ is obtained by the customized FBG sensor unit, and the corresponding working principle is explained as follows. 1) In the free state, $\lambda_p$ and $\lambda_a$ are closely equal and their difference $\Delta\lambda$ is ≈0. 2) When the pressing force is applied to the distal tip as the soft fingers actively grasp an object, $\lambda_p$ varies because of the increase of the air pressure. In this case, $\lambda_a$ is approximately invariable and limited by obstacles. In conclusion, $\Delta\lambda$ can be utilized to reflect the change of the contact force. Two groups of experiments were conducted to verify its feasibility as follows.

### 3.4.1. Prediction of the Pressing Force at the Distal Fingertip

A force sensor was placed at a distance of 0, 15, and 30 mm from the distal tip of the soft finger as the obstacle to investigating the fingertip pressing force prediction respectively (Figure 9b). During the bending and deformation process of the soft finger, the pressing forces, $\lambda_p$ and $\lambda_a$, were recorded at the same time (Figure 9c). The dotted and solid lines of the same color represented the predicted wavelength $\lambda_p$ and the actual wavelength $\lambda_a$ and the intersection point of them indicated the first contact

between the soft finger and the force sensor. The experimental results show that the difference between $\lambda_p$ and $\lambda_a$ increased as the pressing force raised. This experiment demonstrated the potential of the soft finger to predict the pressing force at the distal tip.

### 3.4.2. Hardness Recognition and Grasping Process Perception

The soft gripper was utilized in three grasping experiments in free space, with a sponge cylinder, and a light-cured resin cylinder respectively (**Figure 10**a). The values of $p$ and $\lambda_a$ were obtained through the sensors and $\lambda_p$ was calculated by the ANN2 model at the same time and the results are shown in Figure 10b. The $\lambda_p$ of the single-deformed soft finger in free space is illustrated in the green line in Case-p. For the experiment in free space, the purple line represents the change of FBG wavelength, and there is a turning point (P2) on the purple line, indicating the time when the soft fingers contact each other without loading. Before contacting, Case-f1 of the purple line coincides with the predicted FBG wavelength (green line, Case-p). When these two soft fingers came into contact, their distal tip movement was limited, so the slope of the line decreased significantly (Case-f2). For the grasping experiment with a sponge, the blue line represents the change of FBG wavelength
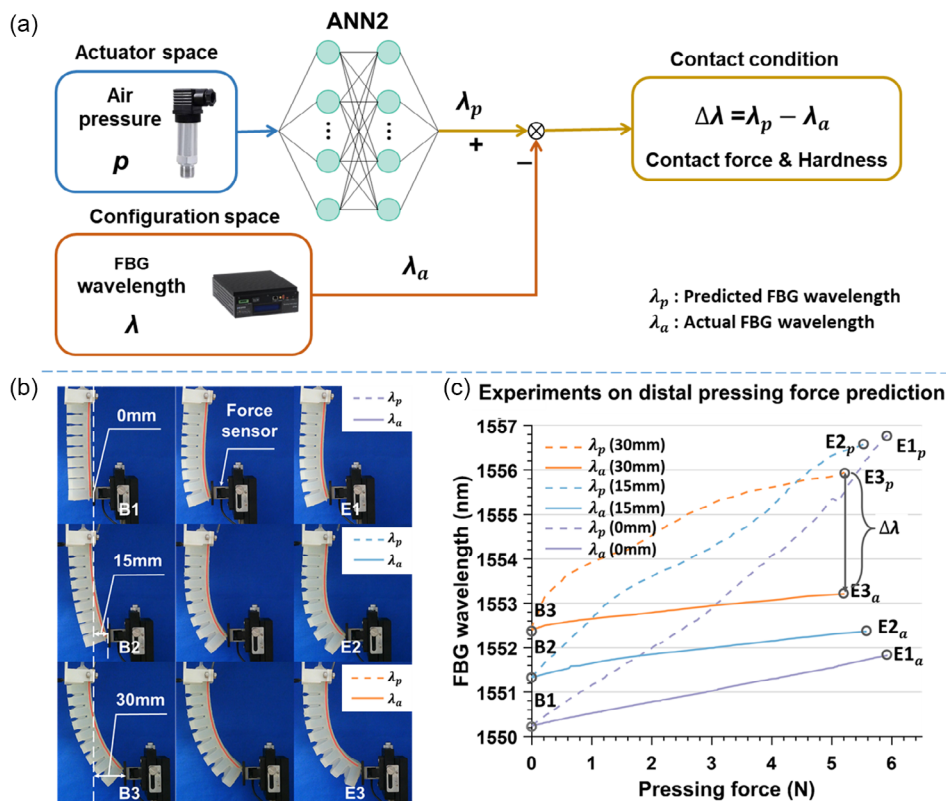
**2200324 (8 of 12)**

**Figure 9.** a) Preliminary contact force perception based on the ANN2 model. b) Experiments on distal pressing force prediction. c) Experimental data of distal pressing force prediction. (Note: B1, B2, and B3 represent the actual FBG wavelength data when the soft finger contacts the force sensor at the initial moment. $E1_a$, $E2_a$, and $E3_a$ represent the actual FBG wavelength data when the air pressure of the soft finger reaches the maximum (the driving cylinder of the soft finger moves to the limit position). $E1_p$, $E2_p$, and $E3_p$ represent the predicted FBG wavelength data by the ANN2 model when the air pressure of the soft finger reaches the maximum.) Please note the labels in b) correspond to the same labels in c) for easy understanding.

**Table 2.** Detailed parameters of the ANN2 model.

| Neural network model | Hidden layer number | Input nodes | Layer1 nodes | Layer2 nodes | Output nodes | Activation function | Learning rate | Training epochs |
|---|---|---|---|---|---|---|---|---|
| ANN2 | 2 | 1 | 64 | 64 | 1 | Relu | 0.2 | 2200 |

and consists of two stages of Case-s1 and Case-s2. In Case-s1, the contact force on the soft gripper was caused by the overall shape deformation of the hollow sponge cylinder. P1 was an inflection point, indicating the time when the central hole of the sponge is compacted by the soft gripper. After that, the contact force was mainly generated by the elastic deformation of sponge material, which was larger than Case-s1, so the slope of the blue line in Case-s2 decreased significantly. For the grasping experiment with a resin cylinder, the orange line represented the change of FBG wavelength, as shown in Case-h. Due to the increase in hardness, its slope was obviously smaller than the purple and blue lines. Thus, the slope values of purple, blue, and orange lines can qualitatively reflect the hardness of the gripped objects to some extent. For instance, the orange line has the smallest slope value and reflects the hard resin cylinder, while the purple line has the largest slope value and reflects the movements in

free space. These results reflect the ability of this method in preliminary hardness recognition and grasping process perception.

### 3.5. Discussion

The comparison among the existing shape estimation method implemented in the pneu-net soft actuators[10,31–35,58–64] has been summarized in **Table 3**. The proposed method based on the ANN model from two sensing modalities supports accurate and robust shape estimation of the pneumatically driven soft finger with an extensive bending angle range and excellent transferability. Compared with these methods, the proposed method achieves an extensive bending angle range of up to 320° (much larger than the previous achievements), achieves an excellent linearity of 99.96%, and realizes a higher accuracy with a relatively low error of 0.69% for the whole shape estimation within this large bending range. The resistance-based stretchable sensors and deformable capacitive sensors are widely utilized, and most of them experience apparent hysteresis and nonlinearity, resulting in low working frequency and limited accuracy. Some implementations can only measure the curvature data but cannot reflect the exact shape.[20,32–34] The liquid metal was introduced to make the stretchable resistive sensor based on the high-precision micro electromechanical system (MEMS) techniques
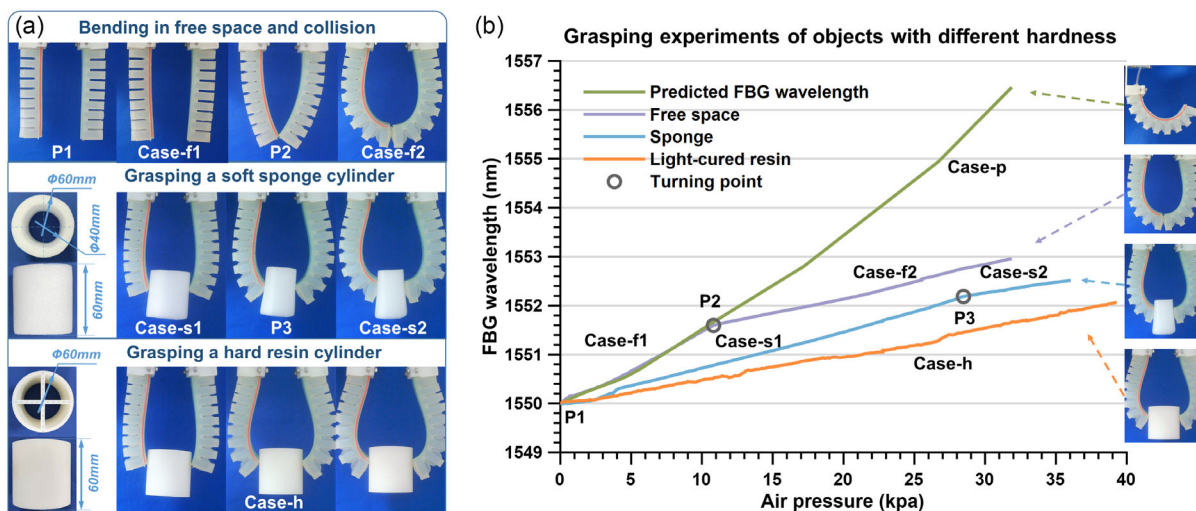
**Figure 10.** a) Experiments on hardness recognition and grasping process perception. b) Experimental data of hardness recognition and grasping process perception. (Note: P1 represents the initial state when the soft finger is not inflated. P2 represents the time when the two soft fingers contact each other without load. P3 represents the moment when the central hole of the sponge is compacted by the soft gripper.) Please note the labels in a) correspond to the same labels in b) for easy understanding.

**Table 3.** The comparison among the existing shape estimation methods implemented in the soft actuators.

| Method | | Sensing functionality | Relative shape reconstruction error | Bending angle measurement range [°] | Linearity | Frequency response [Hz] | Transferability experiment | Refs. |
|---|---|---|---|---|---|---|---|---|
| Sensing transducers | Materials | | | | | | | |
| Resistive | Conductive inks | Curvature | Qualitative | 0–135 | 64% | 2.8 | – | [32] |
| | Saltwater | Curvature | Qualitative | 0–140 | Nonlinearity | 3.665 | – | [33] |
| | Conductive nylon sewing threads | Curvature | Qualitative | 0–60 | – | – | – | [34] |
| | Multiwalled carbon nanotube | Curvature | Qualitative | 0–200 | 96.53% | 1-3 | – | [20] |
| | Conductive textile | Shape | Mean 1.91% Max 4.34% | – | Nonlinearity | – | – | [35] |
| | Liquid metal | Shape | Max 5% | 0–220 | 99.92% | 4 | – | [10] |
| | Multiwalled carbon nanotube | Shape | Max 4.5% | – | Nonlinearity | 10 | – | [58] |
| Capacitive | CB–PDMS | Curvature | Qualitative | 0–70 | Nonlinearity | 1.6 | – | [59] |
| Voltage | Hall effect sensing component | Curvature | Qualitative | – | – | 7.83 | – | [31] |
| | PVDF | Shape | Mean 3% | 0–160 | – | – | – | [60] |
| Optical | FBG | Shape | Mean 1.84% | 0–50 | – | – | – | [61] |
| | FBG | Shape | Min 0.94% Max 15% | 0–70 | – | – | – | [62] |
| | FBG | Shape | Max 2.46% | 0–180 | – | – | – | [63] |
| Learning | | Shape | Mean 1.33% | – | – | – | – | [64] |
| **The proposed method** | | **Shape** | **0.69%(s)[a]** **1.19%(t)[b]** | **0–320** | **99.96%** | **20** | **Supported** | – |

[a]The average relative error for the whole shape; [b]The average relative error for the distal tip.

and achieve a high linearity.[10] However, this design still suffers from the limited working frequency of 4 Hz and achieves the bending angle sensing up to 220°. The FBG optical fibers have been increasing applied to achieve shape reconstruction of soft manipulators with higher accuracy due to their tiny sizes,

excellent flexibility, and multiple-point strain measurement capacity.[40] However, the embedded optical fiber-based shape sensing in soft robots typically is from fiber slippage, the tiny stretchable characteristic, and chirping failure. Therefore, this type of method suffers from a limited bending/motion range

(50°, 70°, and 180° in Table 3),[61–63] poor accuracy for large deformation detection and low transferability due to the direct fiber pasting along the soft manipulator. Some implementations designed the shape-sensing units by attaching glass/silica FBG fibers entirely into a flexible tube made of composite materials[65] or other low-modulus materials[66,67] to realize the shape sensing of the continuum robots, joint movement monitoring, and slip surface monitoring of a landslide. The compliant/soft substrates of these flexible tubes will lower the strain transfer coefficient between the target object and the sensing fiber and improve the sensing range but with the sacrifice of the bending sensing accuracy. These sensing units can be applied for bending with a small length change or fixed length (pure bending), making it difficult to be utilized for the pneumatic-driven soft fingers, where the stretching and bending deformation of typically occur simultaneously. However, the proposed FBG sensor unit has addressed such difficulties. The proximal end of the FBG sensor unit is fixed, and the distal end is set free to slide and synchronize with the extended length. This design can effectively avoid fiber sliding and breakage when bending and well reflect the actual shape with large deformation. The utilization of the long-grating FBG element can further avoid chirping failure associated with the typical FBG element when the soft manipulator experiences a large deformation/bending angle. The designed soft finger in the current work possesses a limited bending angle of 320°, but the detection angle range of our proposed design can be more extensive. The transferability experiments that utilized a newly fabricated soft finger and a newly assembled FBG sensor unit have been performed to maintain accuracy stability without a model training process. Therefore, the proposed method with multiple inputs demonstrates excellent transferability for shape estimation, which can significantly reduce the influences associated with manual fabrication and assembly errors and model uncertainties and further avoid the complex sensor calibration process. The proposed FBG sensor unit design supports convenient integration with various soft manipulators and generates high sensory data repeatability. It produces negligible effects on the bending performances of soft manipulators and thus can further serve as a modular unit for 2D shape estimation. The FBG sensor unit can support the working frequency of 1000 Hz; however, the limitation lies in the working frequency of the commercial air pressure sensor (20 Hz). Thus, the working frequency can be further improved via the change of the air pressure sensor. The FBG optical fiber is a type of quasidistributed sensor that can support both one-point and multiple-point strain measurements to achieve both force and shape-sensing implementations. The FBG fiber can be integrated with the force-sensitive flexure to design the force sensor and achieve distal force sensing.[68,69] The configuration of multiple FBG elements in one optical fiber enables distributed strain and curvature measurements with higher accuracy and supports achieving shape sensing for soft manipulators and continuum robots with more complex shapes.

## 4. Conclusion

A 2D shape estimation method for a pneumatically driven soft finger that adopts two sensing modalities has been proposed and implemented with the ANN model to achieve high-accuracy prediction of the whole shape and distal end position with a large bending motion range. The proposed customized FBG sensor unit is effectively extended onto different soft manipulators, supports the convenient assembly, and generates negligible interferences with the bending performances, demonstrating a modular sensory design for shape sensing. A series of experiments were conducted, and the results demonstrated that the whole shape of the soft finger could be accurately predicted in real time by the proposed method. The transferability on a newly fabricated soft finger has been validated with high accuracy to further improve the robustness of the proposed shape estimation. Future work will extend the current sensor design and develop FBG-based force sensors to realize contact force detection of soft manipulators. Meanwhile, more FBG elements, multicore optical fibers, or other distributed fiber optic strain sensors based on the optical frequency domain reflectometry (OFDR) technology will be applied along the sliding nitinol rod to achieve both force and shape sensing for soft manipulators.

## Conflict of Interest

The authors declare no conflict of interest.

## Data Availability Statement

The data that support the findings of this study are available from the corresponding author upon reasonable request.

[1] M. Pan, C. Yuan, X. Liang, T. Dong, T. Liu, J. Zhang, J. Zou, H. Yang, C. Bowen, *Adv. Intell. Syst.* **2022**, *4*, 2100140.

[2] C. Laschi, B. Mazzolai, M. Cianchetti, *Sci. Rob.* **2016**, *1*, eaah3690.

[3] C. M. Thalman, T. Hertzell, H. Lee, in *2020 3rd IEEE Int. Conf. on Soft Robotics (RoboSoft)*, IEEE, New Haven, CT, **2020**, pp. 801–807.

[4] J. Zhu, L. Lyu, Y. Xu, H. Liang, X. Zhang, H. Ding, Z. Wu, *Adv. Intell. Syst.* **2021**, *3*, 2100011.

[5] M. Runciman, A. Darzi, G. P. Mylonas, *Soft Rob.* **2019**, *6*, 423.

[6] M. Brancadoro, M. Manti, F. Grani, S. Tognarelli, A. Menciassi, M. Cianchetti, *Front. Rob. AI* **2019**, *6*, 12.

[7] J. Shintake, V. Cacucciolo, D. Floreano, H. Shea, *Adv. Mater.* **2018**, *30*, 1707035.

[8] K. C. Galloway, K. P. Becker, B. Phillips, J. Kirby, S. Licht, D. Tchernov, R. J. Wood, D. F. Gruber, *Soft Rob.* **2016**, *3*, 23.

[9] Y. Yang, Y. Zhang, Z. Kan, J. Zeng, M. Y. Wang, *Soft Rob.* **2020**, *7*, 292.

[10] Z. Xie, F. Yuan, Z. Liu, Z. Sun, E. M. Knubben, L. Wen, *IEEE/ASME Trans. Mechatron.* **2020**, *25*, 1841.

[11] N. El-Atab, R. B. Mishra, F. Al-Modaf, L. Joharji, A. A. Alsharif, H. Alamoudi, M. Diaz, N. Qaiser, M. M. Hussain, *Adv. Intell. Syst.* **2020**, *2*, 2000128.

[12] D. Rus, M. T. Tolley, *Nature* **2015**, *521*, 467.

[13] M. S. Xavier, C. D. Tawk, A. Zolfagharian, J. Pinskier, D. Howard, T. Young, J. Lai, S. M. Harrison, Y. K. Yong, M. Bodaghi, A. J. Fleming, *IEEE Access* **2022**, *10*, 59442.

[14] T. da Veiga, J. H. Chandler, P. Lloyd, G. Pittiglio, N. J. Wilkinson, A. K. Hoshiar, R. A. Harris, P. Valdastri, *Prog. Biomed. Eng.* **2020**, *2*, 032003.

[15] S. I. Rich, R. J. Wood, C. Majidi, *Nat. Electron.* **2018**, *1*, 102.

[16] H. Wang, M. Totaro, L. Beccai, *Adv. Sci.* **2018**, *5*, 1800541.

[17] O. Atalay, A. Atalay, J. Gafford, H. Wang, R. Wood, C. Walsh, *Adv. Mater. Technol.* **2017**, *2*, 1700081.

[18] S. E. Navarro, S. Nagels, H. Alagi, L.-M. Faller, O. Goury, T. Morales-Bieze, H. Zangl, B. Hein, R. Ramakers, W. Deferme, G. Zheng, C. Duriez, *IEEE Robot. Autom. Lett.* **2020**, *5*, 5621.

[19] X. Li, J. Guo, X. Ma, L. Yang, K.-M. Lee, C. Xiong, *Soft Rob.* **2021**, *8*, 164.

[20] R. Liu, S. Wang, H. Yang, C. Shi, *IEEE Sens. J.* **2021**, *21*, 23880.

[21] Y. Li, C. Zheng, S. Liu, L. Huang, T. Fang, J. X. Li, F. Xu, F. Li, *ACS Appl. Mater. Interfaces* **2020**, *12*, 23764.

[22] W. Dong, L. Yang, G. Fortino, *IEEE Sens. J.* **2020**, *20*, 8073.

[23] T. Mori, H. Onoe, in *2021 IEEE 34th Int. Conf. on Micro Electro Mechanical Systems (MEMS)*, IEEE, Gainesville, FL, **2021**, pp. 775–778.

[24] H. Zhao, K. O'Brien, S. Li, R. F. Shepherd, *Sci. Rob.* **2016**, *1*, eaai7529.

[25] W. Chen, C. Xiong, C. Liu, P. Li, Y. Chen, *Soft Rob.* **2019**, *6*, 495.

[26] K. C. Galloway, Y. Chen, E. Templeton, B. Rife, I. S. Godage, E. J. Barth, *Soft Rob.* **2019**, *6*, 671.

[27] M. Amanzadeh, S. M. Aminossadati, M. S. Kizil, A. D. Rakić, *Measurement* **2018**, *128*, 119.

[28] K. Bronnikov, A. Wolf, S. Yakushin, A. Dostovalov, O. Egorova, S. Zhuravlev, S. Semjonov, S. Wabnitz, S. Babin, *Opt. Express* **2019**, *27*, 38421.

[29] M. Luo, E. H. Skorina, W. Tao, F. Chen, S. Ozel, Y. Sun, C. D. Onal, *Soft Rob.* **2017**, *4*, 117.

[30] H. Wang, G. de Boer, J. Kow, M. Ghajari, A. Alazmani, R. Hewson, P. Culmer, *Procedia Eng.* **2016**, *168*, 650.

[31] S. Ozel, N. A. Keskin, D. Khea, C. D. Onal, *Sens. Actuators A: Phys.* **2015**, *236*, 349.

[32] A. Koivikko, E. Sadeghian Raei, M. Mosallaei, M. Mantysalo, V. Sariola, *IEEE Sens. J.* **2018**, *18*, 223.

[33] T. Helps, J. Rossiter, *Soft Rob.* **2018**, *5*, 175.

[34] J. Zhao, A. Abbas, in *ASME 2016 Dynamic Systems and Control Conf.*, American Society Of Mechanical Engineers, Minneapolis, Minnesota, **2016**, p. V002T26A006.

[35] M. Cianchetti, F. Renda, A. Licofonte, C. Laschi, in *2012 4th IEEE RAS & EMBS International Conference on Biomedical Robotics and Biomechatronics (BioRob)*, IEEE, Rome, Italy, **2012**, pp. 634–639.

[36] T. Hoshi, H. Shinoda, in *2008 SICE Annual Conf.*, IEEE, Chofu, Japan, **2008**, pp. 915–920.

[37] P. Mittendorfer, G. Cheng, in **2012** *IEEE/RSJ Int. Conf. on Intelligent Robots and Systems*, IEEE, Vilamoura-Algarve, Portugal, **2012**, pp. 4505–4510.

[38] Y. Lu, W. Chen, B. Li, B. Lu, J. Zhou, Z. Chen, Y.-H. Liu, *IEEE Trans. Med. Rob. Bionics* **2023**, 1.

[39] Y. Lu, B. Lu, B. Li, H. Guo, Y. Liu, *IEEE Rob. Autom. Lett.* **2021**, *6*, 4835.

[40] C. Shi, X. Luo, P. Qi, T. Li, S. Song, Z. Najdovski, T. Fukuda, H. Ren, *IEEE Trans. Biomed. Eng.* **2017**, *64*, 1665.

[41] W. Dou, G. Zhong, J. Cao, Z. Shi, B. Peng, L. Jiang, *Adv. Mater. Technol.* **2021**, *6*, 2100018.

[42] R. J. Webster, B. A. Jones, *Int. J. Rob. Res.* **2010**, *29*, 1661.

[43] D. Trivedi, C. D. Rahn, W. M. Kier, I. D. Walker, *Appl. Bionics Biomech.* **2008**, *5*, 99.

[44] G. Alici, T. Canty, R. Mutlu, W. Hu, V. Sencadas, *Soft Rob.* **2018**, *5*, 24.

[45] Z. Liu, F. Wang, S. Liu, Y. Tian, D. Zhang, *IEEE/ASME Trans. Mechatron.* **2021**, *26*, 2195.

[46] Y. Hao, T. Wang, Z. Ren, Z. Gong, H. Wang, X. Yang, S. Guan, L. Wen, *Int. J. Adv. Rob. Syst.* **2017**, *14*, 172988141770714.

[47] T. George Thuruthel, E. Falotico, M. Manti, A. Pratesi, M. Cianchetti, C. Laschi, *Soft Rob.* **2017**, *4*, 285.

[48] J. Hao, D. Song, C. Hu, C. Shi, *IEEE Sens. J.* **2023**, *23*, 10836.

[49] B. Shih, D. Shah, J. Li, T. G. Thuruthel, Y.-L. Park, F. Iida, Z. Bao, R. Kramer-Bottiglio, M. T. Tolley, *Sci. Rob.* **2020**, *5*, eaaz9239.

[50] T. L. T. Lun, K. Wang, J. D. L. Ho, K.-H. Lee, K. Y. Sze, K.-W. Kwok, *IEEE Rob. Autom. Lett.* **2019**, *4*, 1454.

[51] I. M. Van Meerbeek, C. M. De Sa, R. F. Shepherd, *Sci. Rob.* **2018**, *3*, eaau2489.

[52] B. Mosadegh, P. Polygerinos, C. Keplinger, S. Wennstedt, R. F. Shepherd, U. Gupta, J. Shim, K. Bertoldi, C. J. Walsh, G. M. Whitesides, *Adv. Funct. Mater.* **2014**, *24*, 2163.

[53] R. V. Martinez, J. L. Branch, C. R. Fish, L. Jin, R. F. Shepherd, R. M. D. Nunes, Z. Suo, G. M. Whitesides, *Adv. Mater.* **2013**, *25*, 205.

[54] M. S. Xavier, A. J. Fleming, Y. K. Yong, *Adv. Intell. Syst.* **2021**, *3*, 2000187.

[55] H. Li, M. Li, K. Ogusu, Y. Sheng, J. Rothenberg, *Opt. Express* **2006**, *14*, 3152.

[56] C. Hnatovsky, D. Grobnic, S. J. Mihailov, *Opt. Express* **2018**, *26*, 23550.

[57] J.-S. Heo, J.-H. Chung, J.-J. Lee, *Sens. Actuators A: Phys.* **2006**, *126*, 312.

[58] J. So, U. Kim, Y. B. Kim, D.-Y. Seok, S. Y. Yang, K. Kim, J. H. Park, S. T. Hwang, Y. J. Gong, H. R. Choi, *Cyborg. Bionic Syst.* **2021**, *2021*, article no. 9843894.

[59] R. P. Rocha, P. A. Lopes, A. T. de Almeida, M. Tavakoli, C. Majidi, *J. Micromech. Microeng.* **2018**, *28*, 034001.

[60] Y. Shapiro, G. Kosa, A. Wolf, *IEEE/ASME Trans. Mechatron.* **2014**, *19*, 1260.

[61] Z. Zhang, X. Wang, S. Wang, D. Meng, B. Liang, in *2018 IEEE Int. Conf. on Robotics and Biomimetics (ROBIO)*, IEEE, Kuala Lumpur, **2018**, pp. 978–983.

[62] H. Yin, H. Zhang, J. Wang, J. Cao, *IEEE Sensors J.* **2020**, *21*, 2951.

[63] T. Li, L. Qiu, H. Ren, *IEEE/ASME Trans. Mechatron.* **2020**, *25*, 406.

[64] Q. Zhao, J. Lai, K. Huang, X. Hu, H. K. Chu, *IEEE/ASME Trans. Mechatron.* **2022**, *27*, 2511.

[65] S. C. Ryu, P. E. Dupont, in *2014 IEEE Int. Conf. on Robotics and Automation (ICRA)*, IEEE, Hong Kong, **2014**, pp. 3531–3537.

[66] L. Li, R. He, M. S. Soares, S. Savovic, X. Hu, C. Marques, R. Min, X. Li, *IEEE Sens. J.* **2021**, *21*, 26793.

[67] K. Wang, S. Zhang, J. Chen, P. Teng, F. Wei, Q. Chen, *Sensors* **2017**, *17*, 2486.

[68] Z. Tang, S. Wang, M. Li, C. Shi, *IEEE Trans. Med. Rob. Bionics* **2022**, *4*, 145.

[69] K. Sun, M. Li, S. Wang, G. Zhang, H. Liu, C. Shi, *IEEE Sens. J.* **2021**, *21*, 16681.